INTERNATIONAL JOURNAL FOR NUMERICAL METHODS IN FLUIDS, VOL. 16, 365–390 (1993)

# COMPARISONS OF TVD SCHEMES FOR TURBULENT TRANSONIC PROJECTILE AERODYNAMICS COMPUTATIONS WITH A TWO-EQUATION MODEL OF TURBULENCE

HERNG LIN† AND CHING-CHANG CHIENG*

*National Tsing Hua University, Hsinchu, Taiwan, Republic of China*

## SUMMARY

The development of a computer program to solve the axisymmetric full Navier–Stokes equations with $k$–$\varepsilon$ two-equation model of turbulence using various total variation diminishing (TVD) schemes is the primary interest of this study. The computations are performed for the turbulent, transonic, viscous flow over a projectile with/without supporting sting at zero angle of attack. The predicted results, as well as the convergence characteristics, by various TVD schemes are compared with each other. The results show that the TVD schemes of higher-order accuracy do have influence on the regions of high gradients such as shock, base corner and base flow. However, the schemes of third-order accuracy do not necessarily improve the agreement with measured data (which is not available on the base) than that of second-order accuracy, but surely generate apparent different result of base flow. The supporting sting on the projectile base will complicate the base flow and the existence of the sting will slightly shift the shock location and slightly change the flow field after the shock. More iteration steps are needed to get the converged results in the computation for the projectile with sting.

KEY WORDS TVD schemes Full Navier–Stokes equation Two-equation model Transonic turbulent flow Projectile aerodynamics Recirculation flow

## INTRODUCTION

Turbulence modelling in the calculation of aerodynamic behaviour of projectiles is an important issue. The conventional Navier–Stokes solvers employ the algebraic eddy viscosity model such as Baldwin–Lomax model,[1] which limits the applicability of Navier–Stokes solver, especially for complex flows. Two equation models of turbulence are very popular in solving complex, incompressible, turbulent flows in various engineering applications. In 1983, Coakley[2] extended these models for flows past aerofoil at angle of attack, later on, numerous investigations[3–9] applied the $k$–$\varepsilon$ turbulence model of similar forms to flows past axisymmetric bump, axisymmetric ramp, aerofoil/wing, cascade, flat plate, compressible corner and backward facing step. The predictions were in good agreement with experiments. In 1985, Sahu and Danberg[10] employed the $k$–$\varepsilon$ two-equation model of turbulence to compute the turbulent flow over projectiles. The

† Graduate Student, Department of Power Mechanical Engineering.
* Professor, Department of Nuclear Engineering, corresponding person.

0271–2091/93/050365–26$18.00

*Received December 1991*
*Revised October 1992*

flowfield over projectiles is a combination of turbulent boundary layer and base flow and the governing equation set is stiff and is difficult to achieve convergence. Therefore, they used a grid system of extended boattail to skip the base flow computation in their work.

In recent years, several computational schemes have been developed to solve the Navier–Stokes equations. Total-Variation-Diminishing (TVD) schemes are the best ones to avoid non-physical oscillations into the solutions, especially near high gradient regions. Gorski *et al.*[13–15] applied the TVD schemes to solve Navier–Stokes equations with the $k$–$\varepsilon$ equations of turbulence and performed the computations for the transonic flowfields over nozzle/afterbody, axisymmetric afterbodies, and six-degree compression corner. In their work, near-wall techniques were employed in the near-wall region to allow high CFL numbers and stabler convergence. In 1989, Takakura[16] solved the flowfield over the ONERA-M6 wing by Harten–Yee[17] TVD scheme with Jones–Launder $k$–$\varepsilon$ turbulence model,[18] i.e. wall functions were abandoned and the flowfield near the wall were also obtained.

Present study uses TVD schemes of various forms to solve Navier–Stokes equations with Chien's $k$–$\varepsilon$ turbulence model[19] and compares the effectiveness and accuracy of various TVD schemes for the transonic turbulent flow past projectiles at zero angle of attack. The computation is performed on the grid systems of a real projectile with a supporting sting or with flat base. The solution with these grid system are much more difficult to achieve convergence than that with the grid system of extended boattail of Sahu.[10]

## GOVERNING EQUATIONS

The differential equations used to describe the mean flow for this study are the time-dependent, mass-averaged Navier–Stokes equations for axisymmetric flow of a compressible fluid. Depending on the turbulence model used, two additional equations of turbulent kinetic energy ($k$) and turbulent energy dissipation rate ($\varepsilon$) are implemented. The two-equation model used here is the Chien's $k$–$\varepsilon$ model,[18] which is similar to that of Jones and Launder.[9] The resulting equations, in divergence or conservation law form, can be written as follows:

$$\partial_t(\hat{Q})+\partial_\xi(\hat{E})+\partial_\eta(\hat{F})=\partial_\xi(\hat{M})+\partial_\eta(\hat{N})+\hat{H}, \tag{1}$$

where $\xi$, $\eta$ are co-ordinates in the longitudinal and circumferential directions, and $t$ is the time. $\hat{Q}$, $\hat{E}$, $\hat{F}$, $\hat{H}$, $\hat{M}$, $\hat{N}$ are $6\times 1$ column matrix and their elements are

$$\hat{Q}=\frac{1}{J}\begin{bmatrix}\rho\\ \rho u\\ \rho v\\ e\\ \rho k\\ \rho\varepsilon\end{bmatrix},\qquad \hat{E}=\frac{1}{J}\begin{bmatrix}\rho U\\ \rho uU+\xi_x p\\ \rho vU+\xi_y p\\ U(e+p)\\ \rho kU\\ \rho\varepsilon U\end{bmatrix},\qquad \hat{F}=\frac{1}{J}\begin{bmatrix}\rho V\\ \rho uV+\eta_x p\\ \rho vV+\eta_y p\\ V(e+p)\\ \rho kV\\ \rho\varepsilon V\end{bmatrix},$$

$$\hat{M}=\frac{M_\infty}{Re_\infty J}\begin{bmatrix}0\\ \tau_{xx}\xi_x+\tau_{xy}\xi_y\\ \tau_{xy}\xi_x+\tau_{yy}\xi_y\\ u(\tau_{xx}\xi_x+\tau_{xy}\xi_y)+v(\tau_{xy}\xi_x+\tau_{yy}\xi_y)+\dot{q}_x\xi_x+\dot{q}_y\xi_y\\ (\mu_l+\mu_t/\sigma_k)(\xi_x k_x+\xi_y k_y)\\ (\mu_l+\mu_t/\sigma_\varepsilon)(\xi_x\varepsilon_x+\xi_y\varepsilon_y)\end{bmatrix},$$

$$\hat{N}=\frac{M_\infty}{Re_\infty J}\begin{bmatrix} 0 \\ \tau_{xx}\eta_x+\tau_{xy}\eta_y \\ \tau_{xy}\eta_x+\tau_{yy}\eta_y \\ u(\tau_{xx}\eta_x+\tau_{xy}\eta_y)+v(\tau_{xy}\eta_x+\tau_{yy}\eta_y)+\dot{q}_x\eta_x+\dot{q}_y\eta_y \\ (\mu_l+\mu_t/\sigma_k)(\eta_x k_x+\eta_y k_y) \\ (\mu_l+\mu_t/\sigma_\varepsilon)(\eta_x \varepsilon_x+\eta_y \varepsilon_y) \end{bmatrix},$$

$$\hat{H}=\frac{1}{J}\begin{bmatrix} 0 \\ 0 \\ p/y+(M_\infty/Re_\infty)\mu_{\text{eff}}(2/3\ \text{div}\ \vec{\mathbf{V}}-2v/y) \\ 0 \\ P-\rho\varepsilon-2(M_\infty/Re_\infty)\mu_l k/y_n^2 \\ c_1(\varepsilon/k)P-c_2\rho\varepsilon^2/k-2(M_\infty/Re_\infty)(\varepsilon/y_n^2)\exp(-0{\cdot}5\,y^+)\mu_l \end{bmatrix},$$

where

$$U=\xi_x u+\xi_y v, \qquad V=\eta_x u+\eta_y v \quad \text{(contravariant velocities)},$$

$$\text{div}\ \vec{\mathbf{V}}=u_x+v_y+v/y,$$

$$\mu_{\text{eff}}=\mu_l\ \text{(molecular part)}+\mu_t\ \text{(turbulent part)}$$

$$\mu_k=\mu_l+\mu_t/\sigma_k, \quad \mu_\varepsilon=\mu_l+\mu_t/\sigma_\varepsilon, \qquad \sigma_k=1{\cdot}0, \quad \sigma_\varepsilon=1{\cdot}3,$$

$$\tau_{xx}=\tfrac{2}{3}\mu_{\text{eff}}(2u_x-v_y-v/y),$$

$$\tau_{yy}=\tfrac{2}{3}\mu_{\text{eff}}(2v_y-u_x-v/y),$$

$$\tau_{xy}=\mu_{\text{eff}}(u_y+v_x),$$

$$u_x=u_\xi\xi_x+u_\eta\eta_x, \qquad u_y=u_\xi\xi_y+u_\eta\eta_y,$$

$$v_x=v_\xi\xi_x+v_\eta\eta_x. \qquad v_y=v_\xi\xi_y+v_\eta\eta_y,$$

$$\dot{q}_x=\kappa[\xi_x\partial_\xi(a^2)+\eta_x\partial_\eta(a^2)],$$

$$\dot{q}_y=\kappa[\xi_y\partial_\xi(a^2)+\eta_y\partial_\eta(a^2)],$$

$$\kappa=(\mu_l/Pr_l+\mu_t/Pr_t)/(\gamma-1),$$

where $P$ is the production of turbulent kinetic energy and is expressed as

$$P=(M_\infty/Re_\infty)\mu_t[2(u_x^2+v_y^2)+2(v/y)^2+(u_y+v_x)^2-(\text{div}\ \vec{\mathbf{V}})^2]-\tfrac{2}{3}\rho k(\text{div}\ \vec{\mathbf{V}}).$$

This constitutes a low Reynolds number formulation of the $k$–$\varepsilon$ model. Calculations are extended up to the wall itself, and exact value of the dependent variables at the wall are used as boundary conditions.

The $k$–$\varepsilon$ model employs the eddy viscosity concept and relates eddy viscosity to the turbulent kinetic energy and dissipation rate as

$$\mu_t=c_\mu\rho(k^2/\varepsilon)(Re_\infty/M_\infty).$$

The empirical coefficients in the turbulence model are:[18]

$$c_1 = 1{\cdot}35,$$
$$c_2 = 1{\cdot}80[1-0{\cdot}22\exp(-R_t^2/36)],$$
$$c_\mu = 0{\cdot}09[1-\exp(-0{\cdot}0115\,y^+)],$$
$$R_t = (Re_\infty/M_\infty)\rho k^2/(\mu\varepsilon).$$

*Numerical algorithm*

The finite volume approach is used for the formulations of difference equations, i.e. the numerical fluxes are defined at cell interfaces and dependent variables are defined at the centroids. The discrete form of equation (1) can be approximated as

$$\hat{Q}_{i,j}^{n+1} - \hat{Q}_{i,j}^{n} = -\frac{\Delta t}{\Delta\xi}[(\tilde{E}-\tilde{M})_{i+1/2,j} - (\tilde{E}-\tilde{M})_{i-1/2,j}]^{n+1} - \frac{\Delta t}{\Delta\eta}[(\tilde{F}-\tilde{N})_{i,j+1/2} - (\tilde{F}-\tilde{N})_{i,j-1/2}]^{n+1} + \hat{H}_{i,j}^{n+1}. \tag{2}$$

When evaluating the numerical flux functions $\tilde{E}_{i\pm1/2,j}$, the metrics are evaluated at $i\pm1/2, j$. Likewise, the metrics are evaluated at $i, j\pm1/2$ for $\tilde{F}_{i,j\pm1/2}$. In this study, the TVD numerical flux is applied for the convective term $(\tilde{E}, \tilde{F})$ and the central difference approximation is used for the viscous term $(\tilde{M}, \tilde{N})$. Four TVD schemes are formulated using finite volume approach. The expressions of the numerical fluxes for these schemes employed in this study are described briefly and the details can be found in the cited references.

*van Leer's third-order MUSCL type TVD scheme*[20, 21]

This scheme extends the original Roe's scheme[20] to third order with MUSCL interpolation by van Leer.[21] The numerical flux can be in terms of

$$\tilde{E}_{i+1/2,j} = \tfrac{1}{2}[\hat{E}(Q_{i+1/2,j}^R) + \hat{E}(Q_{i+1/2,j}^L) - \hat{R}_{i+1/2,j}|\hat{\lambda}|_{i+1/2,j}\hat{\alpha}_{i+1/2,j}], \tag{3}$$

where

$$Q_{i+1/2,j}^L = Q_{i,j} + \frac{s}{4}[(1-\kappa s)(\Delta Q)^- + (1+\kappa s)(\Delta Q)^+]_{i,j},$$

$$Q_{i-1/2,j}^R = Q_{i,j} - \frac{s}{4}[(1-\kappa s)(\Delta Q)^+ + (1+\kappa s)(\Delta Q)^-]_{i,j},$$

$$(\Delta Q)_{i,j}^- = Q_{i,j} - Q_{i-1,j},$$
$$(\Delta Q)_{i,j}^+ = Q_{i+1,j} - Q_{i,j},$$
$$s = [2(\Delta Q)_{i,j}^-(\Delta Q)_{i+1,j}^+ + \varepsilon_0]/[(\Delta Q)_{i,j}^{-2} + (\Delta Q)_{i+1,j}^{+2} + \varepsilon_0],$$

$\kappa = \frac{1}{3}$ for third-order scheme and $\varepsilon_0 = 1{\cdot}0\times10^{-6}$ to avoid dividing by zero.

The Roe's average[20] is used to calculate the right-eigenvector matrix $\hat{R}_{i+1/2,j}$, its inverse $\hat{R}_{i+1/2,j}^{-1}$ and the eigenvalue matrix $|\hat{\lambda}|_{i+1/2,j}$, where $\hat{R}$, $\hat{R}^{-1}$ are $6\times6$ matrices having the forms as

$$R=\begin{bmatrix} r_{11} & r_{12} & r_{13} & r_{14} & 0 & 0 \\ r_{21} & r_{22} & r_{23} & r_{24} & 0 & 0 \\ r_{31} & r_{32} & r_{33} & r_{34} & 0 & 0 \\ r_{41} & r_{42} & r_{43} & r_{44} & 0 & 0 \\ 0 & 0 & 0 & 0 & r_{55} & 0 \\ 0 & 0 & 0 & 0 & 0 & r_{66} \end{bmatrix}, \qquad R^{-1}=\begin{bmatrix} l_{11} & l_{12} & l_{13} & l_{14} & 0 & 0 \\ l_{21} & l_{22} & l_{23} & l_{24} & 0 & 0 \\ l_{31} & l_{32} & l_{33} & l_{34} & 0 & 0 \\ l_{41} & l_{42} & l_{43} & l_{44} & 0 & 0 \\ 0 & 0 & 0 & 0 & l_{55} & 0 \\ 0 & 0 & 0 & 0 & 0 & l_{66} \end{bmatrix},$$

where $[r_{ij}]$, $[l_{ij}]$ $(i=1, 4, j=1, 4)$ are $4\times 4$ model matrices and the inverse matrix $R^{-1}$ for the inviscid mean flow equations has a standard form suggested by Pulliam.[22] $r_{55}, r_{66}, l_{55}$ and $l_{66}$ are the elements of model matrix $R$ and inverse model matrix $R^{-1}$ for $k$ and $\varepsilon$ equations and their values can be given as follows:[14]

$$r_{55}=r_{66}=\rho, \qquad l_{55}=l_{66}=\frac{1}{\rho}.$$

The eigenvalue matrix $[\lambda]_{i+1/2,j}$ in $\xi$-direction can be expressed as

$$[\lambda]=\text{diag}[U, U, U+c(\xi_x^2+\xi_y^2)^{0\cdot 5}, U-c(\xi_x^2+\xi_y^2)^{0\cdot 5}, U, U]$$

and $|\lambda|$ represents the diagonal matrix of which elements are all positive.

$\hat{\alpha}$ is the differential characteristic (Riemann) variable matrix, which is defined as $\hat{\alpha}_{i+1/2,j}=\hat{R}^{-1}_{i+1/2,j}(Q^R_{i+1/2,j}-Q^L_{i+1/2,j})$. This scheme will display third-order accuracy in the smooth region but it is reduced to first-order accuracy near shock or other extreme value region.

*Harten's second-order upwind TVD Scheme*[17]

For this scheme, the numerical flux can be given as

$$(\tilde{E})_{i+1/2,j}=\tfrac{1}{2}(\hat{E}_{i,j}+\hat{E}_{i+1,j}+\hat{R}_{i+1/2,j}\hat{\phi}_{i+1/2,j}), \tag{5}$$

where

$$\hat{\phi}_{i+1/2,j}=\tfrac{1}{2}\Psi(\hat{\lambda}^1_{i+1/2,j})(\hat{g}^1_{i,j}+\hat{g}^1_{i+1,j})-\Psi(\hat{\lambda}^1_{i+1/2,j}+\hat{\gamma}^1_{i+1/2,j})\hat{\alpha}^1_{i+1/2,j}$$

$$\hat{g}^1_{i,j}=\text{minmod}\,(\hat{\alpha}^1_{i+1/2,j}, \alpha^1_{i-1/2,j}),$$

$$\hat{\gamma}^1_{i+1/2,j}=\begin{cases} \dfrac{1}{2}\Psi(\hat{\lambda}^1_{i+1/2,j})\dfrac{\hat{g}^1_{i+1,j}-\hat{g}^1_{i,j}}{\hat{\alpha}^1_{i+1/2,\,j}} & \text{if } \hat{\alpha}^1_{i+1/2,j}\neq 0, \\ 0 & \text{if } \hat{\alpha}^1_{i+1/2,j}=0, \end{cases}$$

$$\Psi(z)=\begin{cases} |z| & |z|\geq\delta_1, \\ (z^2+\delta_1^2)/2\delta_1 & |z|<\delta_1. \end{cases}$$

This scheme is non-MUSCL type second-order upwind TVD scheme and also called 'modified flux scheme'. $\delta_1$ is set as 0·05 in the present computation. The 'minmod' function of a list of arguments is equal to the smallest absolute value of these arguments if the arguments are of the same sign, or is equal to zero if any arguments are of opposite sign.

The function $\Psi(z)$ is an entropy correction to $z$ and $\hat{g}^1_{i,j}$ is the 'limiter' function. $\hat{E}_{i,j}$ and $\hat{E}_{i+1,j}$ are evaluated with matrices computed at $i+1/2, j$. $\hat{R}_{i+1/2,j}$ is the matrix of right eigenvectors of the Jacobian matrix $\partial\hat{E}/\partial\hat{Q}$ evaluated using Roe's averaged variables, and $\phi$ is a vector that contains the first-order diffusion and second-order correction terms.

*Yee's second-order symmetric TVD scheme*[23]

The numerical flux function, $\tilde{E}_{i+1/2,j}$, is defined as

$$\hat{E}_{i+1/2,j}=\tfrac{1}{2}[\hat{E}_{i,j}+\hat{E}_{i+1,j}+\hat{R}_{i+1/2,j}\hat{\phi}_{i+1/2,j}]. \tag{6}$$

The above terms have the same definitions as those in the Harten's scheme except $\hat{\phi}_{i+1/2,j}$ is expressed as

$$\hat{\phi}_{i+1/2,j}=-\Psi(\hat{\lambda}_{i+1/2,j})(\hat{\alpha}_{i+1/2,j}-\hat{W}_{i+1/2,j}),$$
$$\hat{W}_{i+1/2,j}\equiv\text{minmod}\,(\alpha_{i-1/2,j},\alpha_{i+1/2,j},\alpha_{i+3/2,j}).$$

*Roe's first-order scheme*[20]

The numerical flux can be in terms of

$$\tilde{E}_{i+1/2,j}=\tfrac{1}{2}[\hat{E}(Q_{i,j})+\hat{E}(Q_{i+1/2,j})-\hat{R}_{i+1/2,j}|\hat{\lambda}|_{i+1/2,j}\hat{\alpha}_{i+1/2,j}]. \tag{7}$$

*Time differencing*

The implicit approximately factored backward-Euler scheme for the full Navier–Stokes equations and $k$–$\varepsilon$ equations that use upwind differencing in the $\xi$- and $\eta$-direction can be written in the following form[21,24]

$$[I+\Delta t(\partial_\xi^-\hat{A}^+ +\partial_\xi^+\hat{A}^-)]^n[I+\Delta t(\partial_\eta^-\hat{B}^+ +\partial_\eta^+\hat{B}^-)-\Delta t\hat{D}]^n(\Delta\hat{Q})_{i,j}^n=\text{RHS of equation (2) at time } t, \tag{9}$$

where the splitting Jacobian matrix $\hat{A}^+$, $\hat{A}^-$, $\hat{B}^+$, $\hat{B}^-$ are evaluated by model matrices $\hat{R}$, $\hat{R}^{-1}$ and diagonal matrices $[\hat{\lambda}^+]$, $[\hat{\lambda}^-]$, i.e.

$$\hat{A}^+=\hat{R}[\hat{\lambda}^+]\hat{R}^{-1},\qquad \hat{A}^-=\hat{R}[\hat{\lambda}^-]\hat{R}^{-1} \tag{10}$$

and the similar form for $\hat{B}^+$, $\hat{B}^-$. $[\hat{\lambda}^+]$, $[\hat{\lambda}^-]$ are diagonal matrices whose elements are all-positive and all-negative eigenvalues. First-order upwind differencing[24] is employed for evaluating the splitting matrix $\hat{A}^+$, $\hat{A}^-$, $\hat{B}^+$ and $\hat{B}^-$.

Generally, in order to maintain the stability of the viscous term, the modified split Jacobian matrices $\hat{A}_v^\pm$ (or $\hat{B}_v^\pm$) are[2]

$$\hat{A}_v^\pm=\hat{R}^\pm([\hat{\lambda}^\pm]\pm\nu\hat{I})\hat{R}^{-1\pm}$$
$$\nu=\frac{2\gamma M_\infty(\mu_{\text{eff}}/\rho)|\vec{\nabla}\xi|^2}{(Re\,Pr)}. \tag{11}$$

All these Jacobian matrices $\hat{A}_v^\pm$, $\hat{B}_v^\pm$ are evaluated at cell interfaces and replace the $\hat{A}^\pm$ and $\hat{B}^\pm$ in equation (9).

The source term $H$ associated with the turbulence field variables is composed of production, dissipation and decay terms and the values can be very large. It can become dominant over the convection and diffusion terms near the wall. This is the result in a very stiff algorithm if all source terms are treated in an explicit manner. Therefore, an additional $6\times 6$ Jacobian matrix $\hat{D}$ is incorporated on the LHS which is formed by taking partial derivatives of $k$–$\varepsilon$ source terms $H_5, H_6$ with respect to conservative variables $\rho k, \rho\varepsilon$. All the values of elements of $\hat{D}$ except

$d_{55}, d_{56}, d_{65}, d_{66}$ are equal to zero and the values of the non-zero elements are given below

$$\begin{aligned} d_{55} &= 2c_\mu(k/\varepsilon)P' - 2(M_\infty/Re)\mu_1/(\rho y_n^2), \\ d_{56} &= -c_\mu(k^2/\varepsilon^2)P' - 1, \\ d_{65} &= c_1 c_\mu P' + c_2\varepsilon^2/k^2, \\ d_{66} &= -2c_2\varepsilon/k - (M_\infty/Re)[\mu_1 \exp(-0{\cdot}5y^+)/(\rho y_n^2)], \end{aligned} \tag{12}$$

where

$$P' = 2(u_x^2 + v_y^2) + 2(v/y)^2 + (u_y + v_x)^2 - \tfrac{2}{3}(\operatorname{div} \vec{\mathbf{V}})^2,$$

and $c_1$, $c_2$ and $c_\mu$ are empirical constants listed in the previous section.

The matrix $\hat{D}$ is replaced by $\hat{D}'$ to ensure the diagonal dominance in the present work and the values of the elements in $\hat{D}'$ are

$$\begin{aligned} d'_{55} &= d'_{66} = -\max(|d_{55}|, |d_{66}|), \\ d'_{65} &= d'_{56} = 0. \end{aligned} \tag{13}$$

After the above manipulations, the $k$ and $\varepsilon$ equations can be decoupled from other equations. Only two scalar tridiagonal matrix equations along with a $4 \times 4$ block-tridiagonal matrix are solved in the present work. Although this uncoupled approach is not as exact as the $2 \times 2$ block tridiagonal system by Nichols[6] and Sahu.[10] The stability of the solution is greatly improved.

There are several approaches to improve the stability and convergence rate for the system of equations. For example, Takakura[16] changed the values of the elements of model matrices $R$ and $R^{-1}$ by adding non-zero coupled terms to $r_{51-4}$, $r_{61-4}$, $l_{51}$ and $l_{61}$. Thus, the $k$ and $\varepsilon$ equations and the system equations of mean flow are coupled completely and $6 \times 6$ block tridiagonal matrix equations must be solved simultaneously. Shih and Chyu[28] proposed an alternative method to treat the stiff source term when approximate factorization algorithm is employed, i.e. the implicit operator on LHS of equation (2) can be written as

$$\begin{aligned} &[I + \Delta t(\partial_\xi^- \hat{A}^+ + \partial_\eta^- \hat{B}^+) - \Delta t\hat{D}]^n [I - \Delta t\hat{D}]^{-1^n} [I + \Delta t(\partial_\xi^+ \hat{A}^- + \partial_\eta^+ \hat{B}^-) - \Delta t\hat{D}]^n (\Delta\hat{Q})_{i,j}^n \\ &\qquad = \text{RHS of equation (2) at time } t. \end{aligned} \tag{14}$$

If only a steady-state solution is required, one can let $\Delta t$ change in space.[25] Use of space varying $\Delta t$ can be interpreted as an attempt to use a more uniform Courant number throughout the flow field. Changing $\Delta t$ can be effective for grid spacings varied from very fine to very coarse. The formula of space varying time step of finite volume discretization and axisymmetric flow can be given as

$$\Delta t = \frac{\Delta t_{\text{ref}}}{1 + \sqrt{J}}. \tag{15}$$

*Generation of computational grid*

The test problem is chosen as transonic turbulent flows past a secant-ogive-cylinder-boattail projectile (SOCBT) at zero angle of attack. The calculated results are compared with experimental data.[11,12] The projectile model as shown in Figure 1 has a 3-caliber secant-ogive-part (or nose part) followed by a 2·3 caliber cylinder and 0·5-caliber 7-degree boattail. In this study, two types of computational grid are established by using the hyperbolic solver.[26] For both grids, the outer boundary of the flow domain is about 18 calibers from the projectile and an exponential

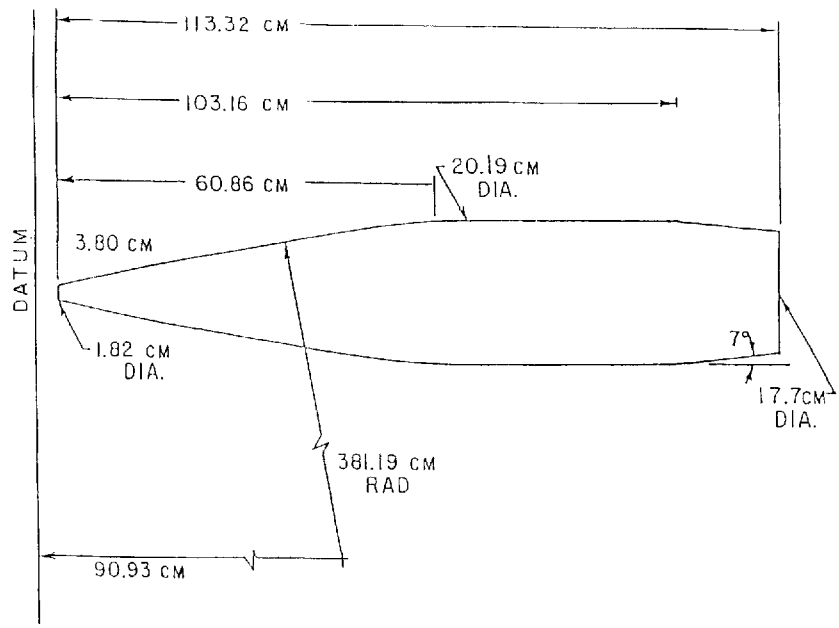


Figure 1. Geometry of secant-ogive-cylinder boattail projectile

stretching function with minimum spacing of 0·00002 caliber from the solid boundary in the hyperbolic grid generations, which provides 2 3-grid point in the viscous sublayer. The first grid shown in Figure 2(a) is $106 \times 60$ O-type grid around the real projectile (i.e. without sting). The boundary for grid points of 1–26–42–76–106 are the point of nose, and connection points for cylinder, boattail and base region. The second grid shown in Figure 2(b) is incorporated with a sting of 0·2 base diameter to support the projectile model in the experiment. The grid in the longitudinal direction is wrapped around the projectile base and sting. There are 30 points between the base corner (5·801 calibers) and the sting corner (5·807 calibers) in the longitudinal direction to approximate the sharp corner of the base. The size of this numerical grid is $142 \times 60$. Similarly, the boundary grid points are distributed as 1–26–42–76–106 142 for secant-ogive, cylinder, boattail and base-sting corner.

*Initial and boundary conditions*

Initial conditions are chosen to be a uniform flow field of free-stream conditions for mean flow equations. The initial conditions to start the $k$–$\varepsilon$ calculations are a uniform field of 2 per cent turbulence intensity:

$$k_0 = 1{\cdot}5(0{\cdot}02 v_\infty)^2, \qquad \varepsilon_0 = k^{1{\cdot}5}/0{\cdot}01,$$

where $v_\infty$ is free-stream speed.

The characteristic extrapolating technique is applied at the far field ($\eta = \eta_{max}$) and outflow positions (i.e. $\xi = \xi_{max}$). The convergence of the present Navier–Stokes solver is reached faster by this method than setting a constant of free-stream value at the far-field boundary. No slip boundary condition is adopted on the solid surface of projectile and sting for velocities $u$ and $v$. The density and pressure on the wall are set to be equal to the values of node points next to the

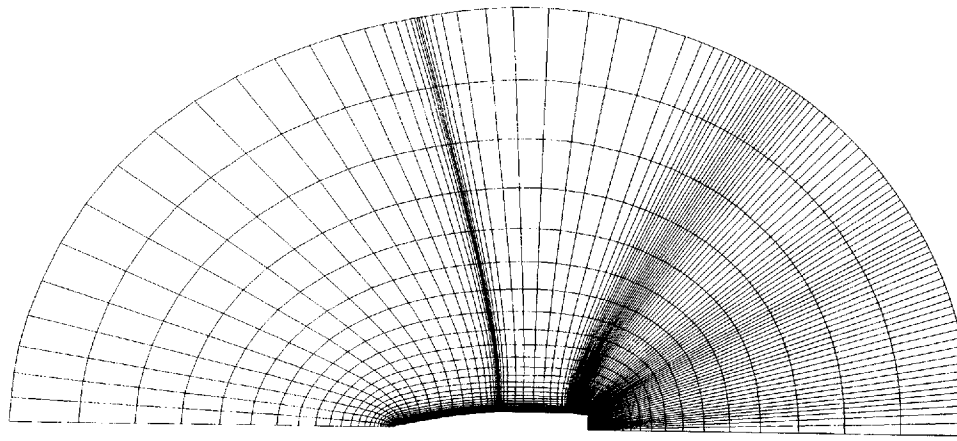

Figure 2(a). A $106 \times 60$ hyperbolic O-type grid

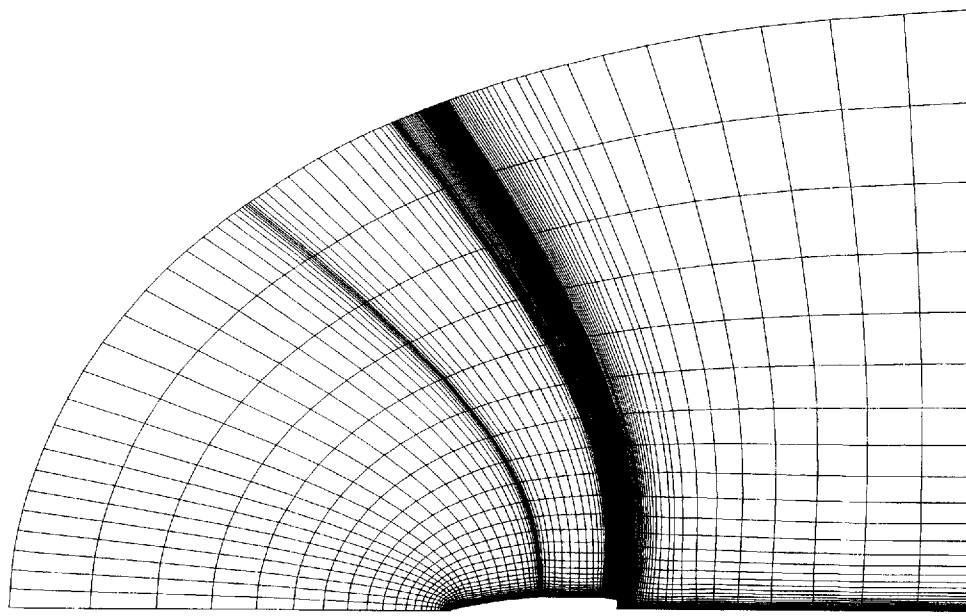

Figure 2(b). A $142 \times 60$ hyperbolic wrapped around grid

wall. It is assumed that the normal momentum equation suggested by Steger[27] need not be solved because the point of $J=2$ is very close to the wall compared to the grid space in longitudinal direction. Axisymmetrical condition at $\xi=1$ is applied.

For the $k$–$\varepsilon$ calculation, a zeroth-order extrapolation of the $k$–$\varepsilon$ values is used to specify conditions at the outflow and symmetric boundary. The turbulent viscosity $\mu_t$ and values of $k$ and $\varepsilon$ are zero or a small value of $10^{-6}$ along solid walls.

## RESULTS AND DISCUSSIONS

Numerical computations have been made for turbulent flow past a secant-ogive-cylinder-boattail projectile at zero angle of attack and for free-streams Mach number of 0·94. The free-stream Reynolds number (defined as $\rho_\infty V_\infty D/\mu_\infty$) is 2,620,000 and is in agreement with the experimental condition. In addition to the mean flow results (such as surface pressure coefficients, velocity profiles on the boattail, the flow patterns surrounding the projectile and behind the base, Mach number contours), the turbulent properties including eddy viscosity $\mu_t$, turbulent kinetic energy $k$ and dissipation rate $\varepsilon$ are obtained by four TVD schemes with two-grid systems. The convergence characteristic of the predictive schemes are also included and compared.

### *Comparisons between different TVD schemes*

*Surface pressure coefficient.* The computed surface pressure coefficients along the projectile for Mach numbers of 0·94 for two-grid systems (i.e. with and without supported sting) are compared with the experimental data.[11,12] Figure 3 shows the computed pressure coefficient by different TVD schemes of different order of accuracy for the case of real projectile of flat base and Mach number 0·94. The schemes are van Leer's third-order MUSCL-type scheme, Yee's second-order symmetric scheme, Harten's second-order scheme and Roe's first-order scheme. The computed values agree with experimental data except $X/L \cong 0{\cdot}6$, but the results by Roe's first-order scheme exhibit the largest difference at all locations. All TVD schemes underpredict pressure values near $X/L = 0{\cdot}63$. This defect is caused by the coarse grids distributed in this region. The results by two second-order TVD schemes and one third-order scheme are of very slight difference along the projectile surface. However, apparent difference for different schemes of different order of accuracy are observed for the surface pressure prediction on the base. This figure also illustrates that the predicted values of surface pressure on the base are converged to the value by higher-

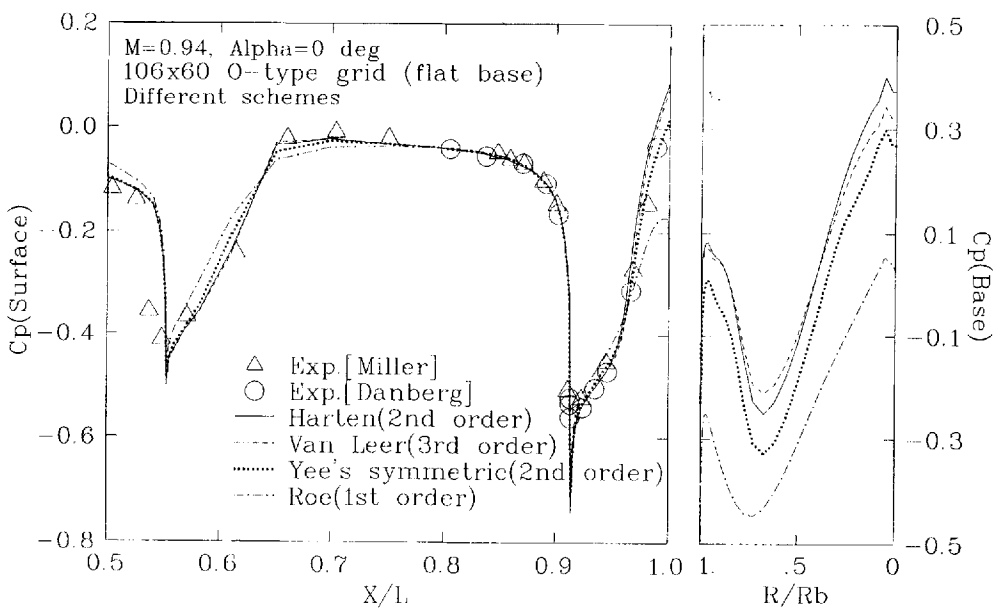


Figure 3. Surface pressure coefficient distributions by different schemes, $M_\infty = 0{\cdot}94$ (base)

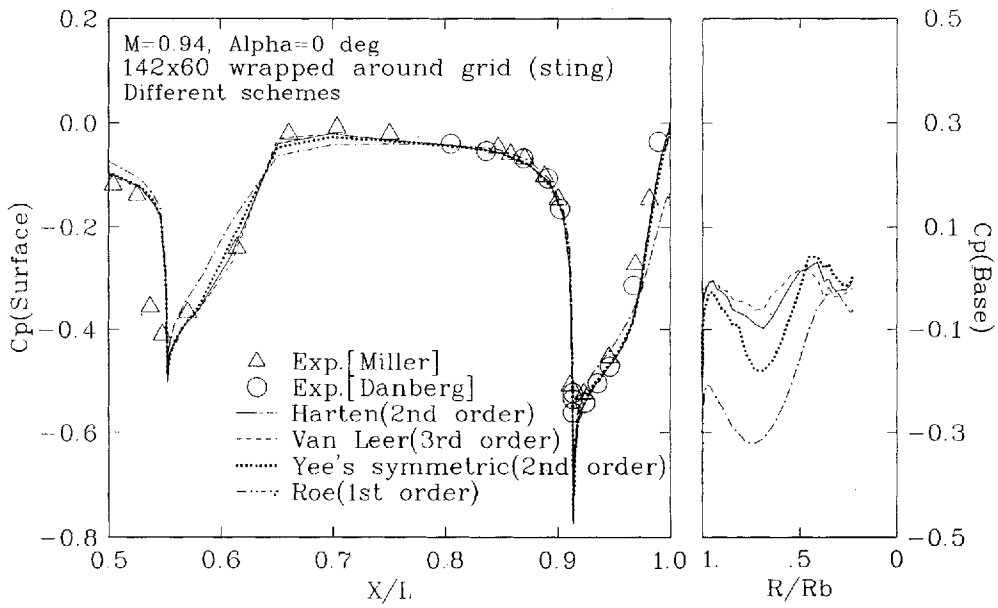


Figure 4. Surface pressure coefficient distributions by different schemes, $M_\infty = 0{\cdot}94$ (sting)

order schemes. Figure 4 shows the comparisons of the measured and predicted surface pressure coefficients by different schemes for the projectile with supporting sting. The computed results for the projectile with supporting sting indicate the same phenomena as that for the projectile with flat base. The pressure coefficients along the projectile surface are very close to the measured values for both the projectiles with and without supporting sting. However, it is also noted that the surface pressure coefficient for the projectile with supporting sting is slightly lower than that for the projectile with flat base near and after the shock on the boattail, which is favourable to the desired results. The small difference is due to the prediction of shock position which is slightly influenced by the flow patterns after the base. The flow field in the base region is complex, existing strong viscous/inviscid interaction, viscous/viscous interaction and regions of large recirculation. Accurate prediction of the flow field in the wake region is very difficult. Higher-order schemes should yield results of better accuracy. It shows that smaller variations of the pressure on the base if higher-order scheme is applied.

*Velocity profile.* The velocity profiles at various axial positions for Mach number 0·94 and the projectile with flat base are shown in Figure 5. The schemes of second and third orders exhibit good agreement with each other at stations $X/L = 0{\cdot}902$, 0·924, 0·946 and 0·967, but give different profiles of the velocity at $X/L = 0{\cdot}989$. Roe's first-order scheme always yield different profiles from others. Figure 6 plots the velocity profiles of the projectile with supporting sting for the same Mach number. It indicates that second or higher-order schemes give the almost same profiles at stations $X/L = 0{\cdot}902$, 0·924, 0·946 and 0·967 and some different profiles at station $X/L = 0{\cdot}989$. The station $X/L = 0{\cdot}967$ is located near the shock for the projectile. The different velocity profiles at $X/L = 0{\cdot}967$ for different base configuration implies that the predicted shock locations for projectiles with and without sting are slightly ahead of $X/L = 0{\cdot}967$ and slightly behind $X/L = 0{\cdot}967$. It can be resulted from the different order of accuracy schemes and different geometries of base yield different flow fields near shocks or rapidly changing region. The

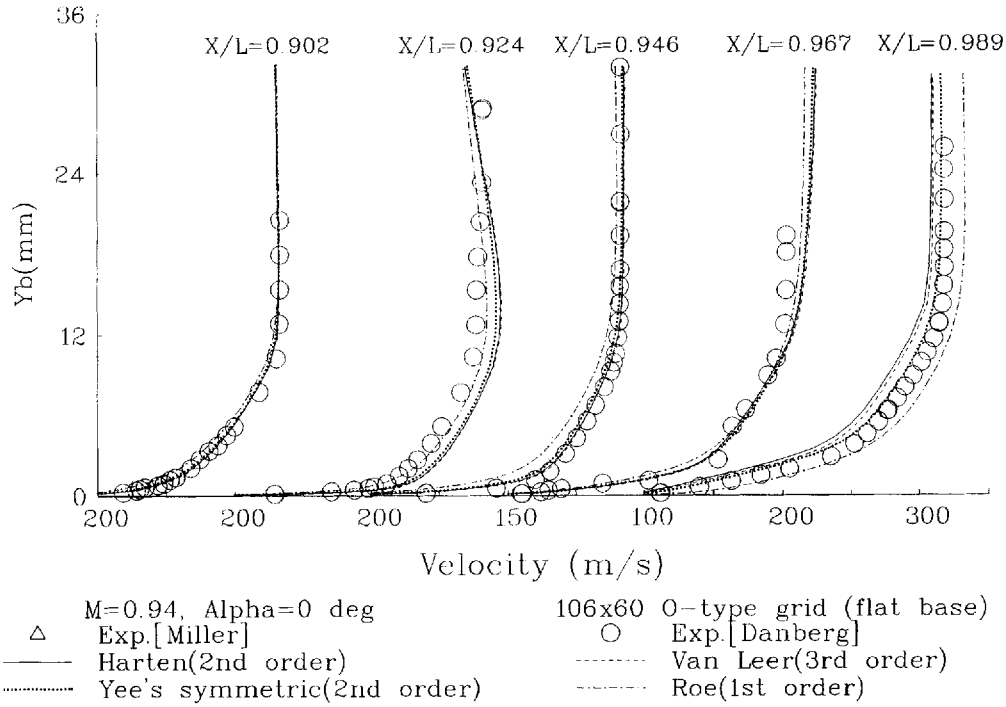


Figure 5. Velocity profiles at various axial station $M_\infty = 0{\cdot}94$ (base)

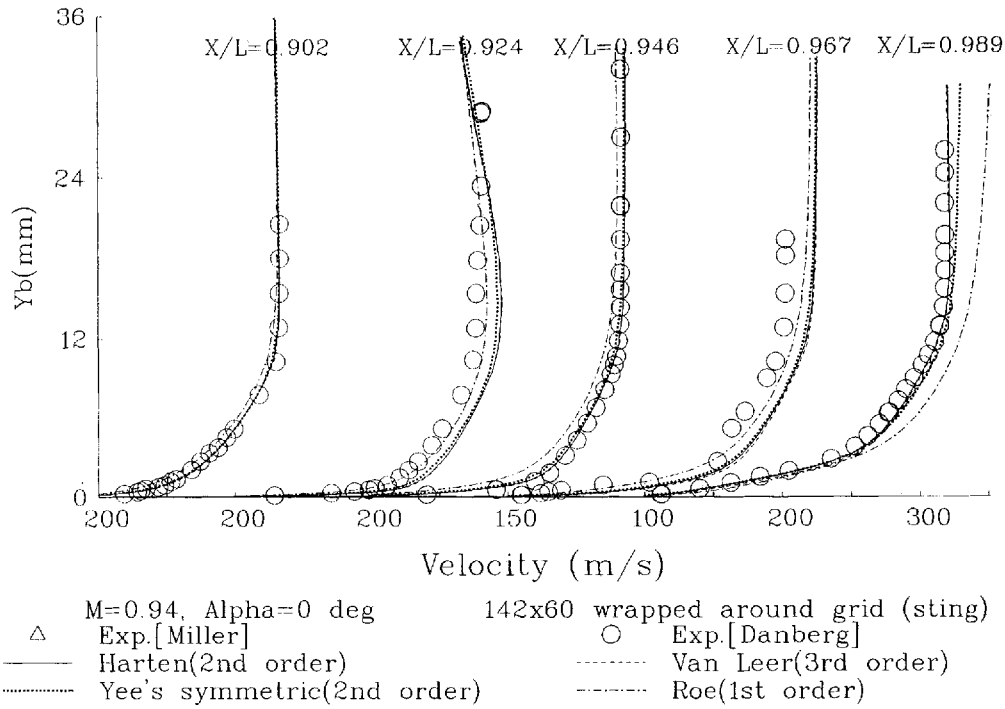


Figure 6. Velocity profiles at various axial station $M_\infty = 0{\cdot}94$ (sting)

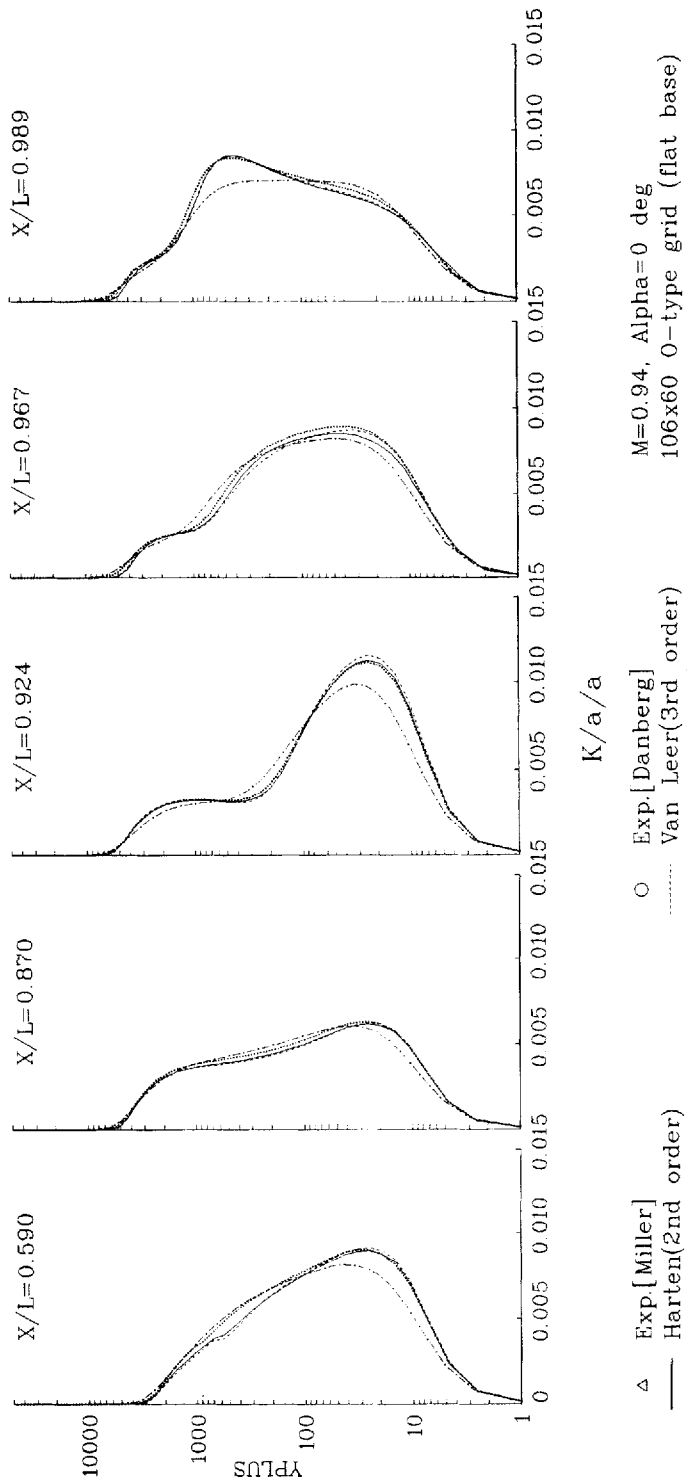


Figure 7. Turbulent kinetic energy profiles at various axial station $M_\infty = 0{\cdot}94$ (base)

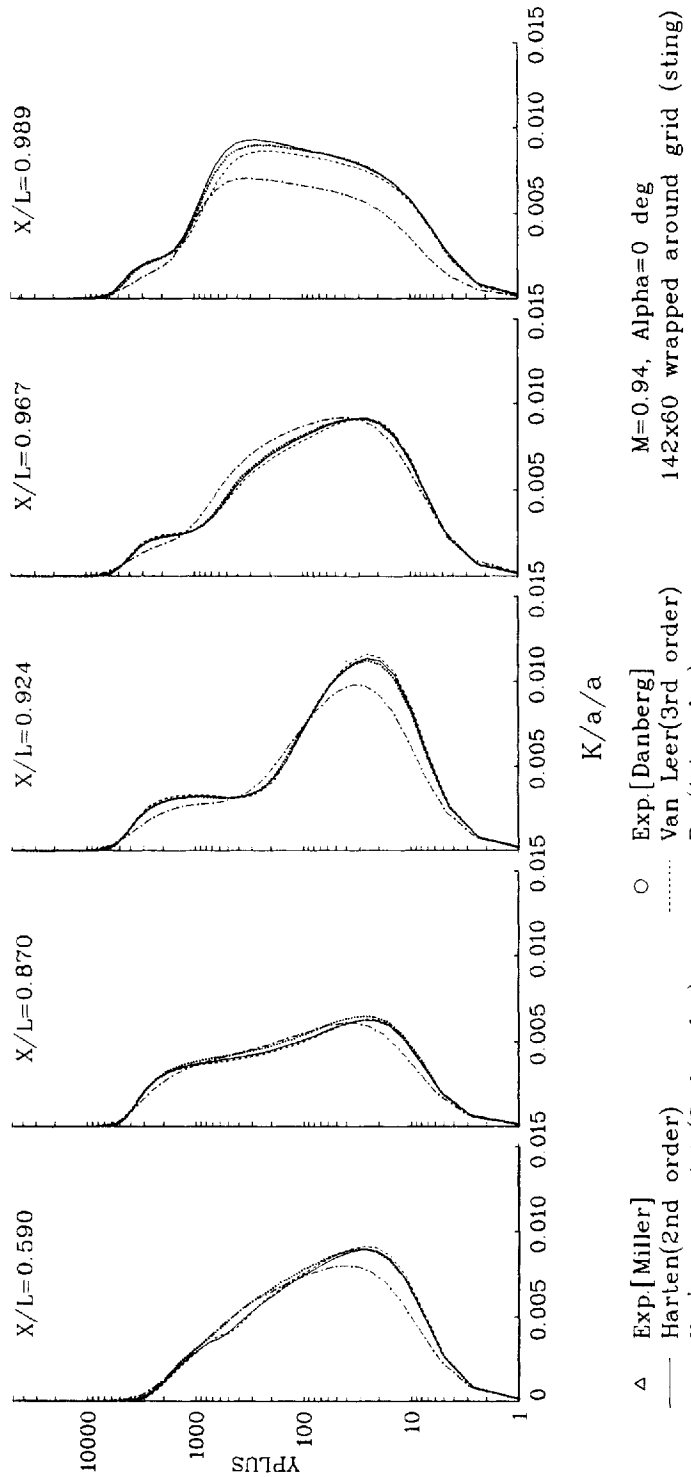


Figure 8. Turbulent kinetic energy profiles at various axial station $M_\infty = 0{\cdot}94$ (sting)

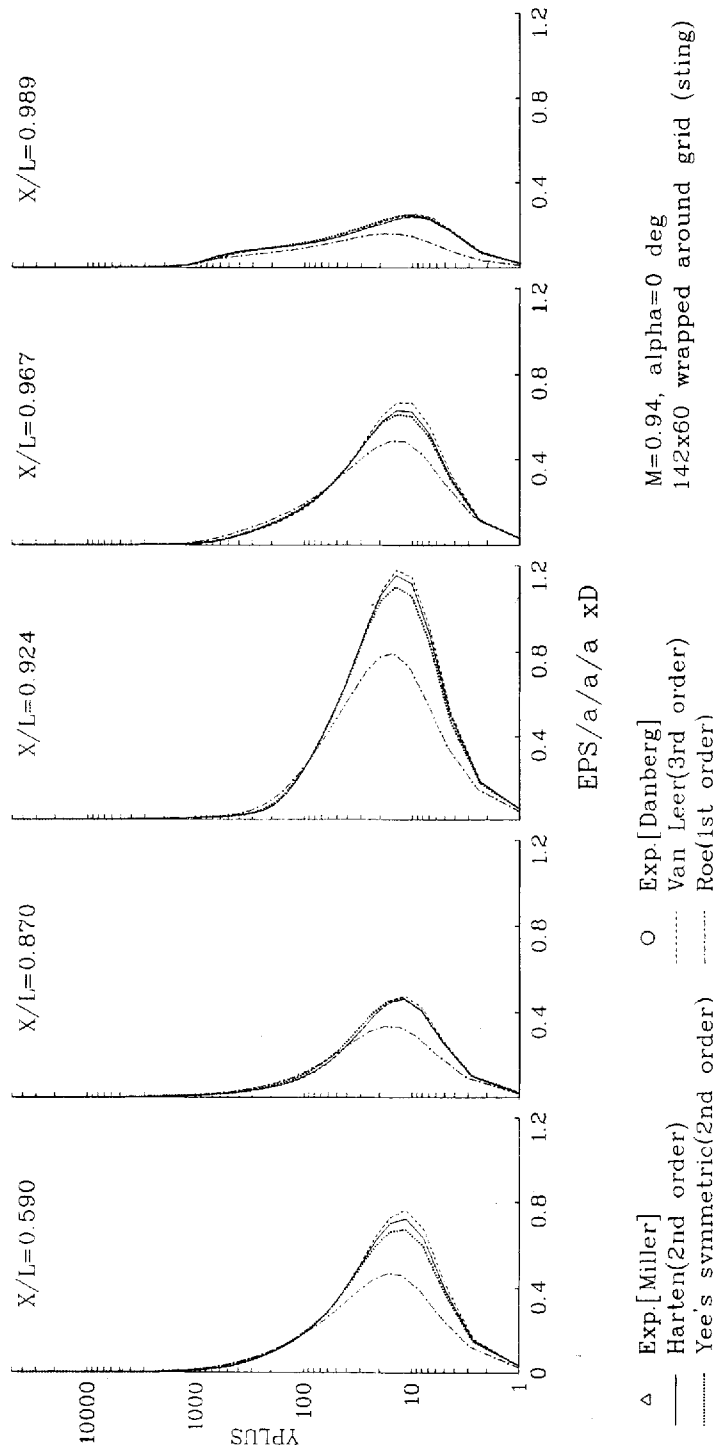


Figure 9. Turbulent dissipation rate profiles at various axial station $M_\infty = 0.94$ (base)

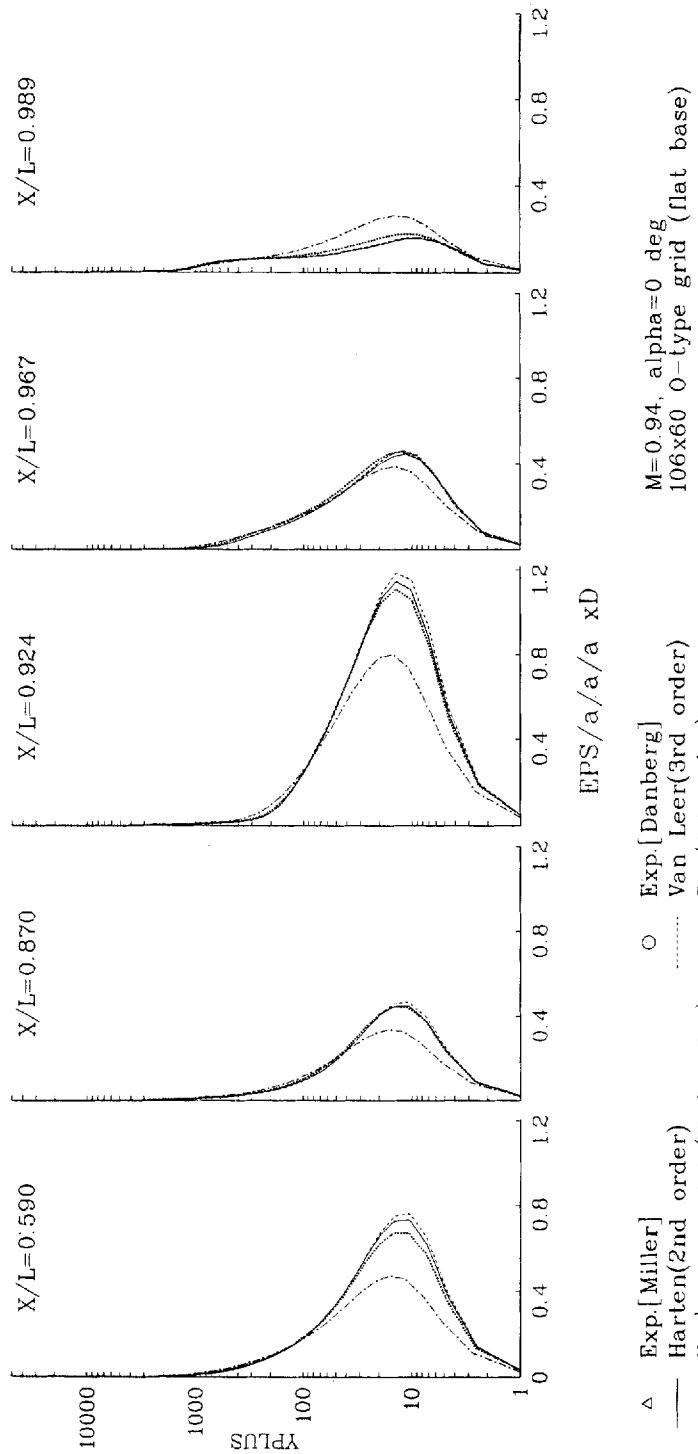


Figure 10. Turbulent dissipation rate profiles at various axial station $M_\infty = 0{\cdot}94$ (sting)

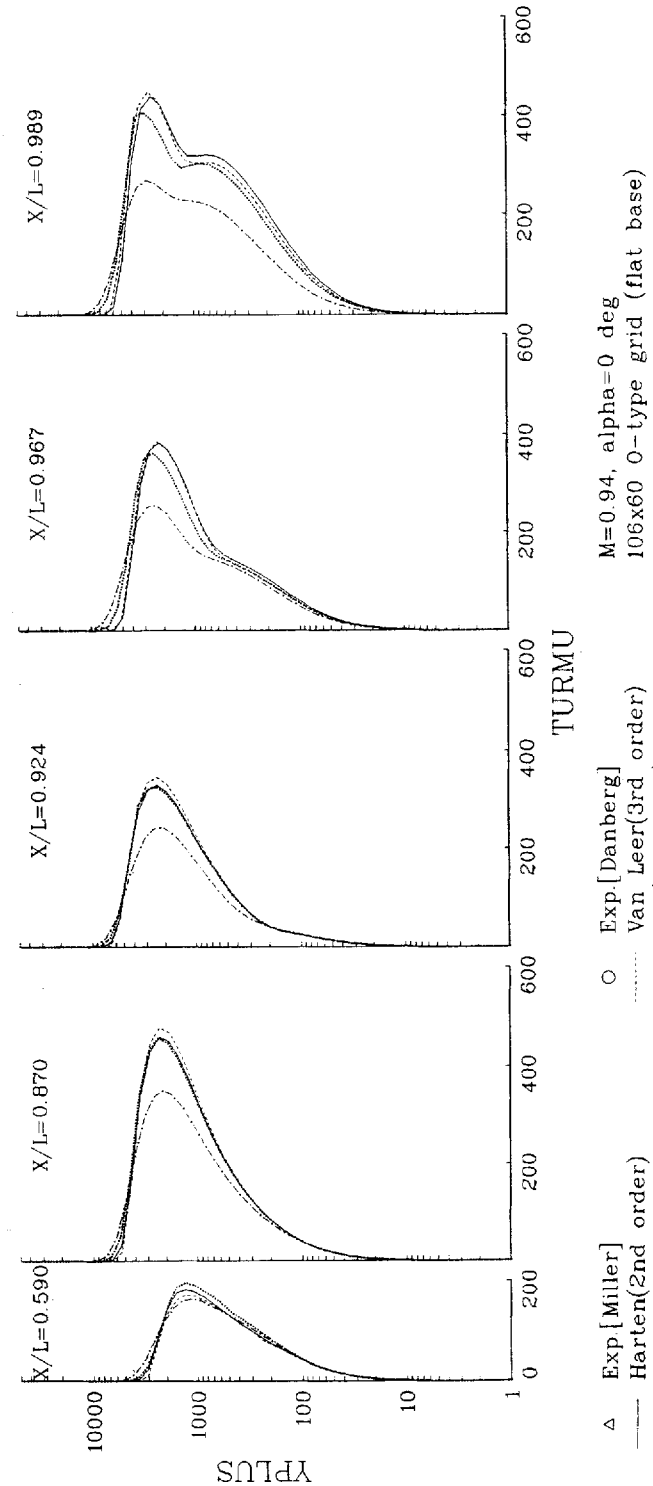


Figure 11. Turbulent viscosity profiles at various axial station $M_\infty = 0{\cdot}94$ (base)

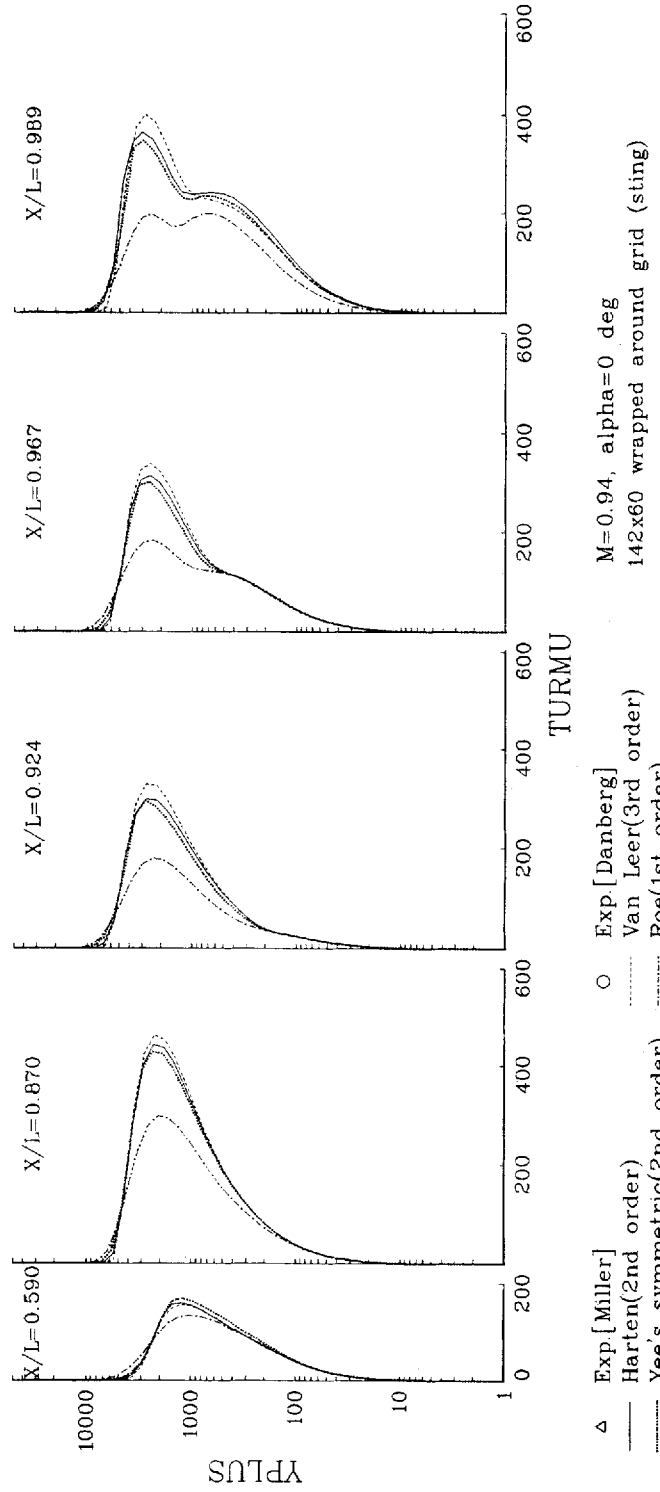


Figure 12. Turbulent viscosity profiles at various axial station $M_\infty = 0{\cdot}94$ (sting)

disagreement with measurement at $X/L=0{\cdot}924$, which is located near the expansion fan, may be related to errors in the reduced measurement data.

*Turbulent quantities.* The turbulent kinetic energy $k$, the rate of turbulent dissipation $\varepsilon$ and eddy viscosity $\mu_t$ profiles along the projectile are of interest. Figures 7 and 8 plot the profiles of turbulent kinetic energy for projectiles with flat base and with supporting sting, respectively. These two figures indicate that results can be categorized in two groups: results by first-order scheme and by higher-order schemes. The profiles generally have peak values near $y^+=40$ and decay rapidly after $y^+>5000$. The magnitude of turbulent kinetic energy is increased due to the expansion fan (comparing profiles at $X/L=0{\cdot}870$ and $0{\cdot}924$) and slightly decreased due to shock (comparing profiles at $X/L=0{\cdot}967$ and $0{\cdot}989$ in Figures 7 and 8). Figures 9 and 10 show the profiles of turbulent energy dissipation rate $\varepsilon$ at various stations for different base configurations. They indicate that the peak value by Roe's scheme is apparently smaller than those by another schemes at five stations. Comparing the profiles of turbulent kinetic energy, the computed profiles of turbulent dissipation rate is more dependent on the selection of numerical schemes. Figures 11 and 12 plot the profiles of turbulent viscosity $\mu_t$ which are important to the computation of mean flow field directly. The results can be divided into two groups also: by first-order scheme and by higher-order schemes. Discrepancies are clearly shown at stations near larger gradients such as near-expansion fan, shock and base corner for higher-order schemes.

*Mach number contour.* The Mach number contours before the base are very similar for two different grid systems and four different TVD schemes. Two represented Mach number contours are shown only in the paper. Figures 13 and 14 show the Mach number contours by third-order

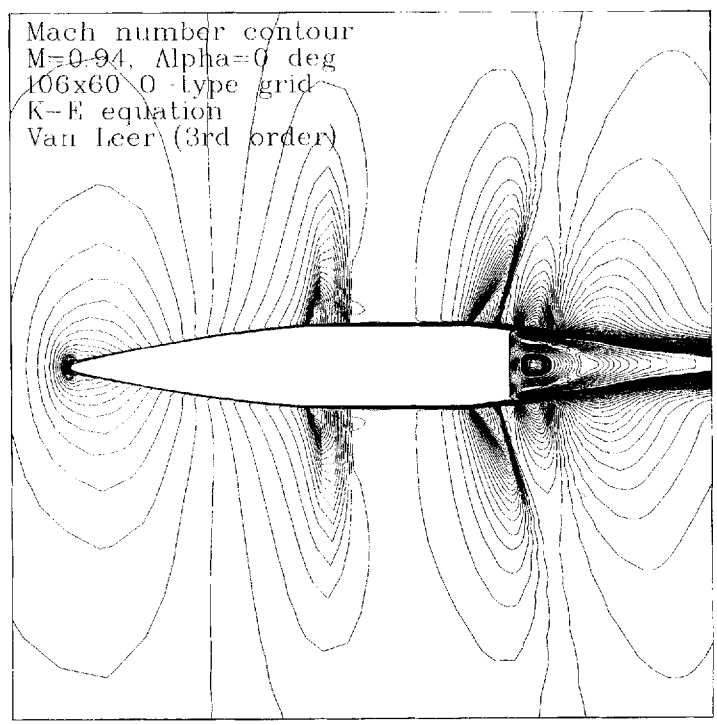


Figure 13. Mach number contour for $M_\infty=0{\cdot}94$ (van Leer's MUSCL, base)

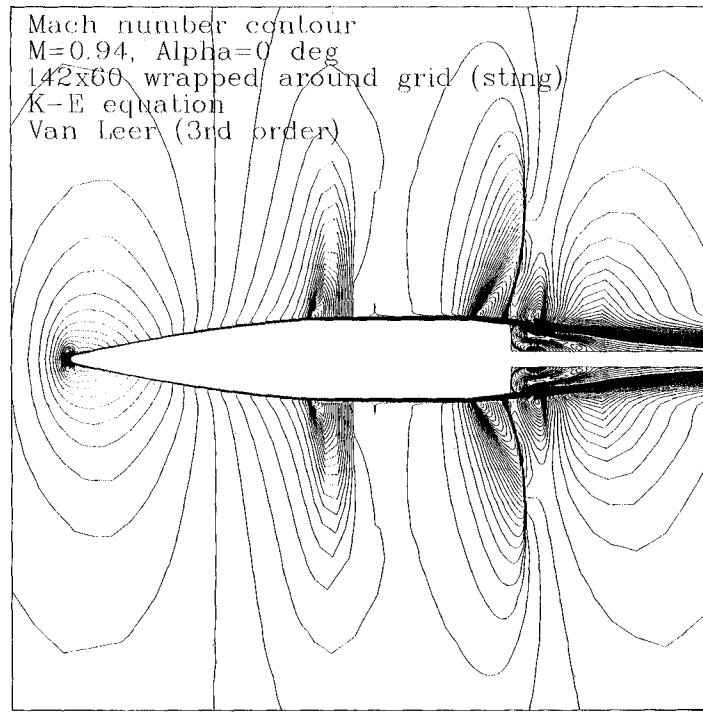


Figure 14. Mach number contour for $M_\infty = 0{\cdot}94$ (van Leer's MUSCL, sting)

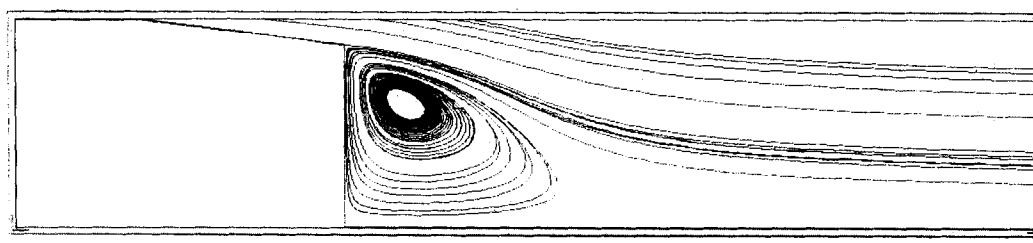

Figure 15(a). Particle tracing plot for $M_\infty = 0{\cdot}94$ (Roe, base)

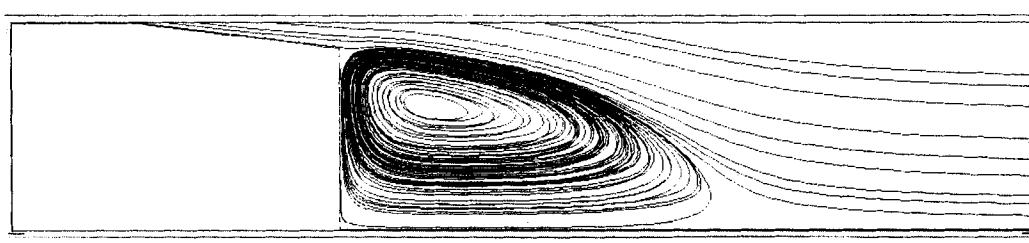

Figure 15(b). Particle tracing plot for $M_\infty = 0{\cdot}94$ (Yee's symmetric, base)

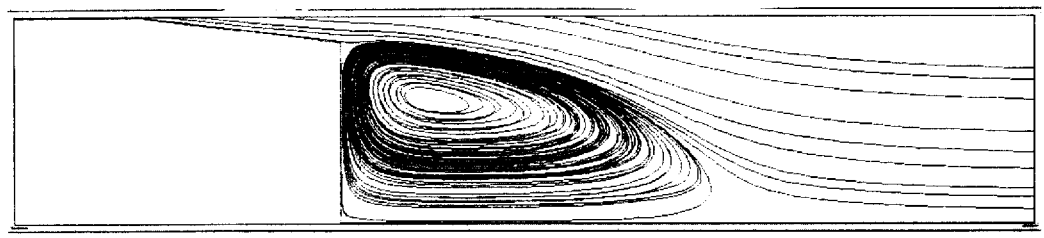

Figure 15(c). Particle tracing plot for $M_\infty = 0{\cdot}94$ (Harten, base)

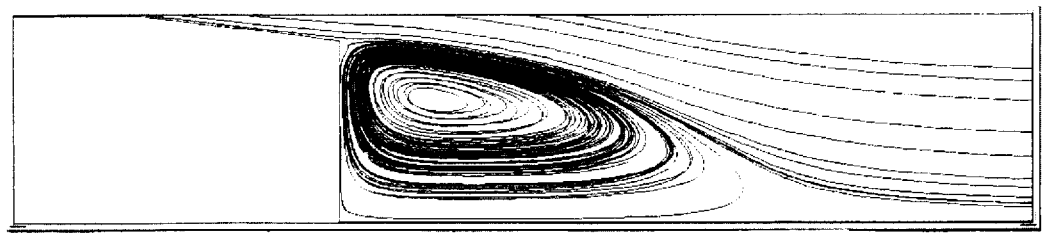

Figure 15(d). Particle tracing plot for $M_\infty = 0{\cdot}94$ (van Leer's MUSCL, base)

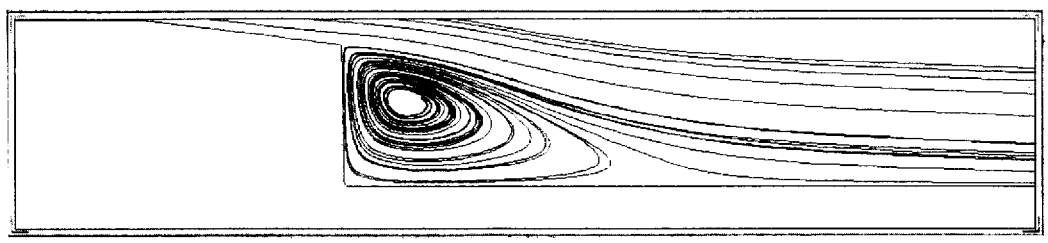

Figure 16(a). Particle tracing plot for $M_\infty = 0{\cdot}94$ (Roe, sting)

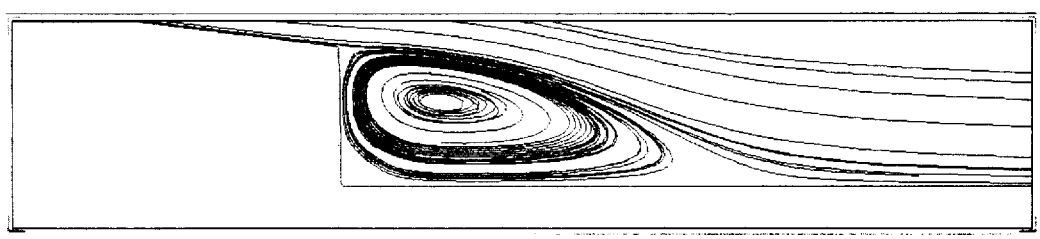

Figure 16(b). Particle tracing plot for $M_\infty = 0{\cdot}94$ (Yee's symmetric, sting)

MUSCL type TVD scheme for the projectile with flat base and with suppporting sting. Very minor difference is observed before the base, but the patterns after the base is completely changed to a much more complicated configuration if the extra supporting sting exists. The contour configurations starting from the shock on the boattail is also influenced and it gives slightly different values of pressure as discussed in the previous section.

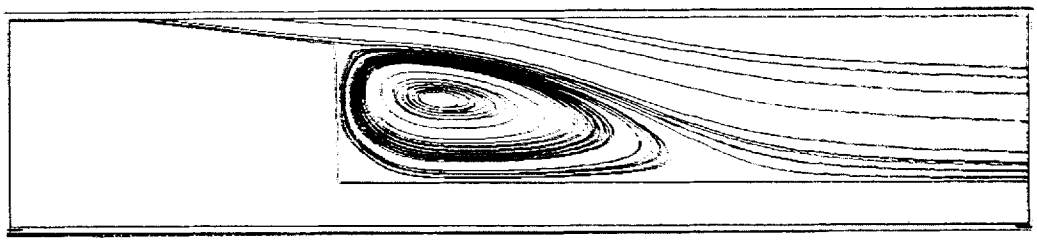

Figure 16(c). Particle tracing plot for $M_\infty = 0{\cdot}94$ (Harten, sting)

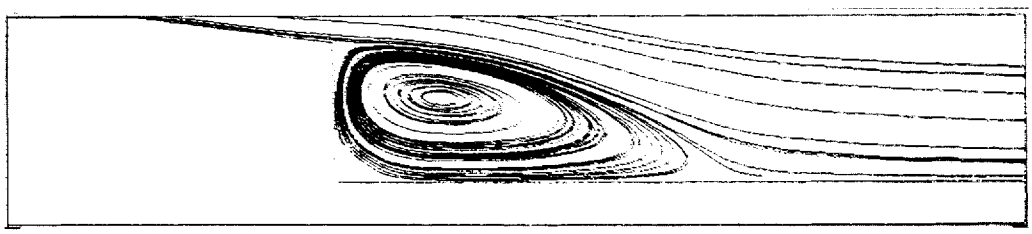

Figure 16(d). Particle tracing plot for $M_\infty = 0{\cdot}94$ (van Leer's MUSCL, sting)

*Recirculation zone.* Figures 15(a)–15(d) show the particle tracing plots in the base region for the projectile with flat base for Mach number 0·94. It is seen that the sizes of recirculation zone are apparently different by the four TVD schemes of different order of accuracy but the centres of the recirculation zones are located nearly the same position for higher-order schemes. If the extra supporting sting is attached to the projectile, the size of the recirculation zones are largely reduced (Figures 16(a)–16(d)). It is observed that the predicted size by Roe's first-order scheme is much smaller than those by higher-order schemes. The secondary vortex regions for the grid system with supported sting are concerned. Figures 16(a)–16(d) indicate that the secondary vortex region by Roe's scheme is smaller than those by another schemes. It can be resulted from the larger numerical diffusions and the smaller vortex in the recirculation zone by the lower-order scheme.

*Iteration history.* The iteration histories with two-grid systems are plotted in Figures 17 and 18. The $L_2$ residual is calculated at each iteration step by the following formulas:

$$\text{Residual} = \sum_{i=1,N_{\text{point}}} [(\Delta Q_1^{(n)}/J)^2 + (\Delta Q_2^{(n)}/J)^2 + (\Delta Q_3^{(n)}/J)^2 + (\Delta Q_4^{(n)}/J)^2]/N_{\text{point}}$$

$$L_2 \text{ residual} = \log_{10}[\text{SQRT(residual)}].$$

It is found that the convergent rate of Roe's first-order scheme is the fastest among the four TVD schemes and that of the third-order scheme is the slowest. All curves exhibit some degree of oscillations within 12 000 iteration steps. The oscillations may be amplified by the strong non-linear property of the two-equation model of turbulence. The $L_2$ residual for all TVD schemes can be reduced over four orders after 7000 iterations and the convergence is actually achieved when five orders are reduced. It means that the convergent rate is very slow if the two equation model of turbulence is implemented. Figure 18 plots the iteration histories for the projectile with supporting sting. Comparing Figures 17 and 18 shows that larger oscillations and

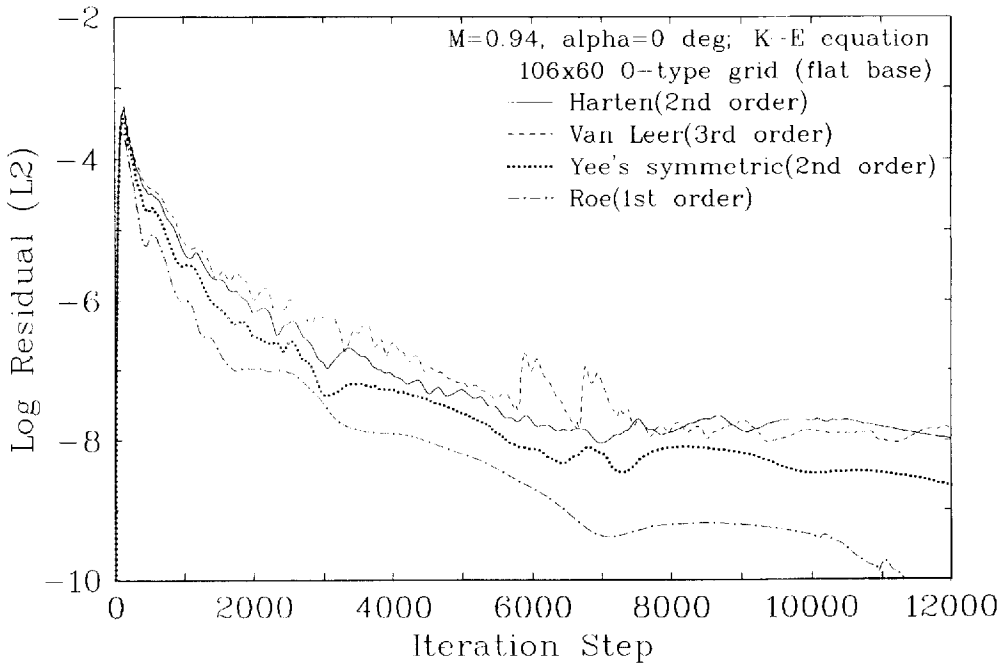


Figure 17. Rate of mean flow residual convergence for $M_\infty = 0{\cdot}94$ (base)

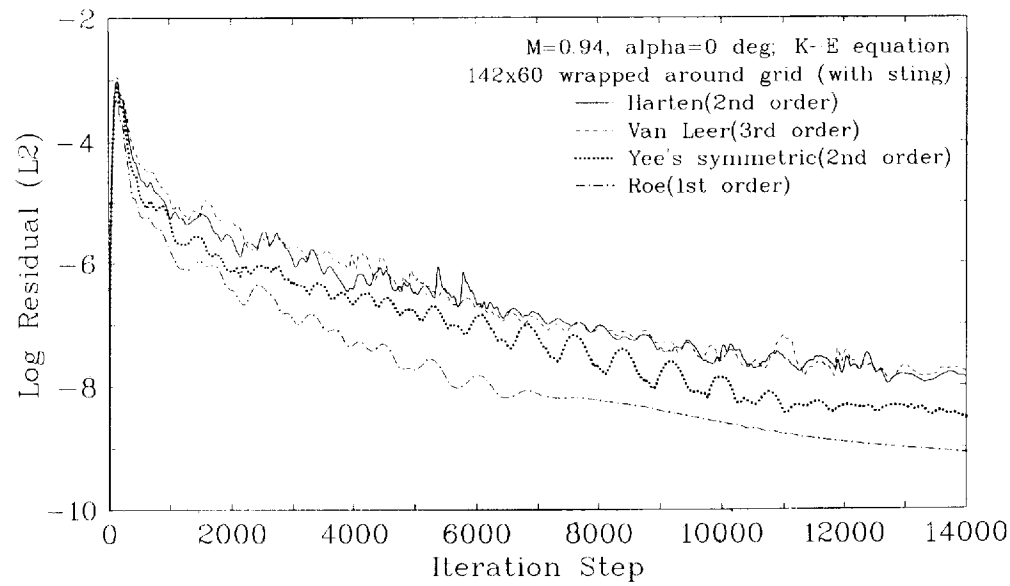


Figure 18. Rate of mean flow residual convergence for $M_\infty = 0{\cdot}94$ (sting)

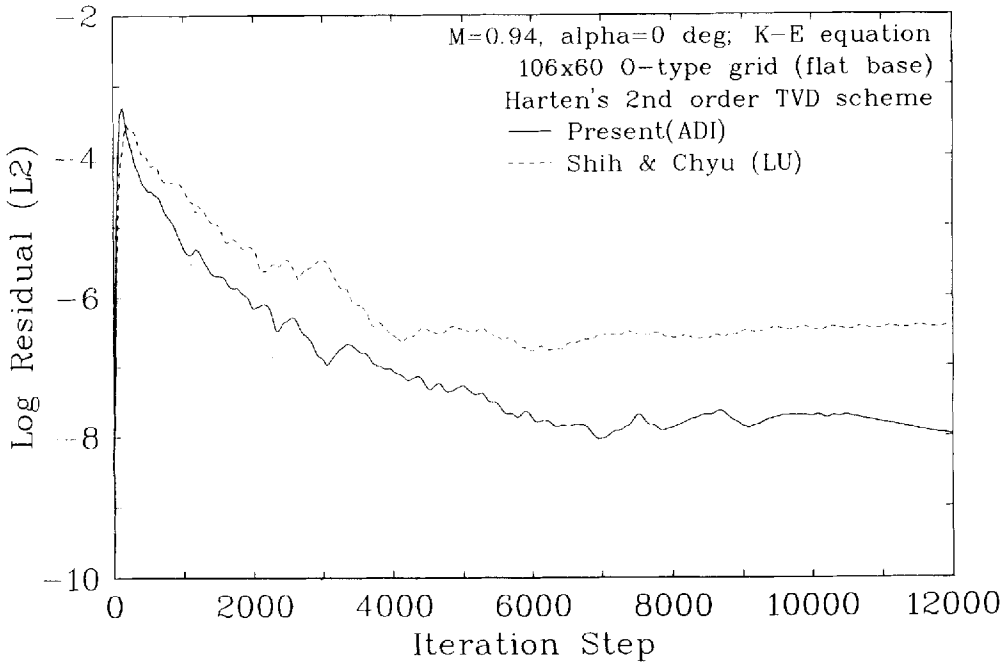


Figure 19. Rate of mean flow residual convergence for $M_\infty = 0{\cdot}94$ (base)

slightly slower converging rate are observed if the supporting sting is adopted to the projectile base.

Figure 19 compares the iteration histories if the present ADI method or the LU method proposed by Shih and Chyu[28] is applied. It shows that the present ADI method has the faster convergent rate than their method has if the same time step is given.

## CONCLUSIONS

Reynolds averaged Navier–Stokes equations with $k$–$\varepsilon$ two-equation model of turbulence are successfully solved by various TVD schemes for transonic turbulent flow over projectiles with and without supporting sting. There are several conclusions which can be made: (1) Very slight differences of the surface pressure coefficients and the profiles of velocity and turbulent quantities on the boattail are observed for the projectile with and without the supporting sting. (2) Most of the computed results can be categorized into two groups: second- and third-order schemes and first-order scheme. Apparent difference is displayed for these two groups. Small discrepancies are obtained for the schemes of second- or higher-order and the discrepancies are found at the locations of high gradients such as shock or base corner. It implies that TVD schemes of second-order accurate is adequate to obtain reasonable flow fields around the projectile (but not the base region). (3) Flow patterns are changed significantly for the base flow computations when TVD schemes of different orders are employed. Different-order schemes will give different sizes of the recirculation zone, the pressure coefficients on the base and, thus, the drag calculation. (4) The pressure coefficients on the base are varied if different TVD schemes are applied. It is found that the computed results of flow patterns and base pressure coefficients are converged from that by first-order scheme to higher-order schemes. It indicates that third- or higher-order scheme is needed for the computation of accurate base flow. (5) The convergence rate for the projectile with

flat base is faster than that for the projectile with supporting sting. The higher-order schemes need more iteration steps to reach convergence.

## APPENDIX: NOMENCLATURE

| | |
|---|---|
| $\hat{E}, \hat{F}, \hat{H}$ | flux vectors in transformed co-ordinates |
| $J$ | Jacobian |
| $k$ | turbulent kinetic energy |
| $L$ | length of the body |
| $M$ | Mach number |
| $\hat{M}, \hat{N}$ | viscous flux vector in transformed co-ordinates |
| $P$ | production rate of turbulent kinetic energy |
| $Pr$ | Prandtl number |
| $Q$ | vector of dependent variables |
| $R_\xi, R_\eta$ | right eigenvector matrix |
| $Re$ | Reynolds number |
| $R_t$ | turbulent Reynolds number |
| $\hat{S}$ | viscous flux vector in transformed co-ordinates |
| $t$ | time |
| $u, v$ | axial and normal velocity components |
| $U, V$ | contravariant velocities in transformed co-ordinates |
| $X$ | distance from projectile nose along the axis of symmetry |
| $x, y$ | axial and radial co-ordinate |
| $y_n$ | normal distance from the solid wall |
| $y^+$ | dimensionless normal distance from the solid wall |

*Greek letters*

| | |
|---|---|
| $\alpha$ | differential characteristic variable vector |
| $\varepsilon$ | turbulent dissipation rate |
| $\gamma$ | ratio of specific heats |
| $\hat{\gamma}$ | modified eigenvalues for upwind TVD scheme |
| $\delta_1$ | small value for entropy correction function $\Psi(z)$ |
| $\kappa$ | parameter for MUSCL type TVD scheme |
| $\mu, \mu_l, \mu_t$ | effective, molecular and turbulent viscosity, $\mu = \mu_l + \mu_t$ |
| $\xi, \eta$ | transformed co-ordinates |
| $\rho$ | density |
| $\phi$ | modified flux function for upwind and symmetric TVD scheme |

*Subscripts*

| | |
|---|---|
| $i \pm 1/2, j \pm 1/2$ | located at the interface of cell |
| $i, j$ | located on centroid of cell |
| $\infty$ | free-stream value |
| l | laminar |
| t | turbulent |

*Superscript*

| | |
|---|---|
| $n$ | time-step level |
| $\tilde{}$ | approximated numerical flux |

| | |
|---|---|
| | any variable including metric terms |
| T | transpose |

## REFERENCES


1. B. S. Baldwin and H. Lomax, 'Thin layer approximation and algebraic model for separated turbulent flows', *AIAA Paper 78-0257*, 1978.
2. T. J. Coakley, 'Turbulence modeling methods for the compressible Navier–Stokes equations', *AIAA Paper 83-1693, AIAA 16th Fluid and Plasma Dynamics Conference*, 1983.
3. J. R. Viegas and M. W. Rubesin, 'On the use of wall function as boundary conditions for two-dimensional separated compressible flows', *AIAA Paper 85-0180, AIAA 23rd Aerospace Science Meeting*, 1985.
4. J. S. Liu, 'Navier–Stokes cascade analysis with a stiff $k$–$\varepsilon$ turbulence solver', *AIAA Paper 88-0594, AIAA 26th Aerospace Science Meeting*, 1988.
5. J. Yokota, 'A diagonally inverted LU implicit multigrid scheme for the 3-D Navier–Stokes equations and a two equation model of turbulence', *AIAA Paper 89-0467, AIAA 27th Aerospace Science Meeting*, 1989.
6. R. H. Nichols, 'A two-equation model for compressible flows', *AIAA Paper 90-0494, AIAA 28th Aerospace Science Meeting*, 1990.
7. U. C. Goldberg and D. Ota, 'A $k$–$\varepsilon$ near-wall formulation for separated flows', *AIAA Paper 90-1482, AIAA 21st Fluid Dynamics, Plasma Dynamics and Lasers Conference*, 1990.
8. D. L. Marcum and R. K. Agarwal, 'A three-dimensional finite element Navier–Stokes solver with $k$–$\varepsilon$ turbulence model for unstructured grids', *AIAA Paper 90-1652, AIAA 21st Fluid Dynamics, Plasma Dynamics and Lasers Conference*, 1990.
9. D. Mavriplis, 'Multigrid solution of compressible turbulent flow on unstructured meshes using a two-equation turbulence model', *AIAA Paper 91-0237, AIAA 29th Aerospace Science Meeting*, 1991.
10. J. Sahu and J. E. Danberg, 'Navier–Stokes computations of transonic flows with a two-equation turbulence model', *AIAA J.*, **24**, 1744–1751 (1986).
11. C. J. Nietubicz, G. R. Inger and J. E. Danberg, 'A theoretical and experimental investigation of a transonic projectile flow field', *AIAA Paper 82-0101, AIAA 20th Aerospace Sciences Meeting*, 1982.
12. M. C. Miller and J. W. Molnar, 'Wind tunnel measurements of the induced surface pressures on a spinning artillery projectile model in the transonic speed regime', Chemical Research, Development and Engineering Center, *CRDEC-TR-86081*, 1986.
13. U. C. Goldberg, J. J. Gorski and S. R. Chakravarthy, 'Transonic turbulent flow computations for axisymmetric afterbodies', *AIAA Paper 85-1639, AIAA 18th Fluid Dynamics, Plasma Dynamics and Lasers Conference*, 1985.
14. J. J. Gorski, S. R. Chakravarthy and U. C. Goldberg, 'High accuracy TVD schemes for the $k$–$\varepsilon$ equations of turbulence', *AIAA Paper 85-1665, AIAA 18th Fluid Dynamics, Plasma Dynamics and Lasers Conference*, 1985.
15. U. C. Goldberg, J. J. Gorski and S. R. Chakravarthy, 'Flowfield computations around nozzle/afterbody configurations at transonic Mach numbers', *AIAA Paper 85-4081, AIAA 3rd Applied Aerodynamics Conference*, 1985.
16. Yoko Takakura, 'Turbulence models for 3D transonic viscous flows', *AIAA Paper 89-1932*, 1989.
17. H. C. Yee and A. Harten, 'Implicit TVD schemes for hyperbolic conservation laws in curvilinear coordinated', *AIAA Paper 85-1513, Proc. AIAA 7th CFD Conference*, 1985.
18. K. Y. Chien, 'Predictions of channel and boundary-layer flows with a low-Reynolds-number turbulence model', *AIAA J.*, **20**, 33–38 (1982).
19. W. P. Jones and B. E. Launder, 'The prediction of laminarization with a two-equation model of turbulence', *Int. J. Heat Mass Transfer*, **15**, 301–314 (1972).
20. P. L. Roe, 'Characteristic-biased schemes for the Euler equations', *Ann. Rev. Fluid Mech.*, **18**, 337–365 (1986).
21. W. K. Anderson, J. L. Thomas and B. Van Leer, 'A comparison of finite volume flux vector splittings for the Euler equations', *AIAA Paper 85-0122. AIAA 23rd Aerospace Sciences Meeting*, 1985.
22. T. H. Pulliam and D. S. Chaussee, 'A diagonal form of an implicit approximate-factorization algorithm', *J. Comput. Phys.*, **39**, 347–363 (1981).
23. H. C. Yee, 'Construction of explicit and implicit symmetric TVD schemes and their applications', *J. Comput. Phys.*, **68**, 151–179 (1987).
24. J. L. Steger and R. F. Warming, 'Flux vector splitting for the inviscid gasdynamics equations with application to finite-difference methods', *J. Comput.*, **40**(2), 263–293 (1987).
25. T. H. Pulliam and J. L. Steger, 'Recent improvements in efficiency, accuracy, and convergence for implicit approximate factorization algorithms', *AIAA Paper 85-0360, AIAA 23rd Aerospace Sciences Meeting*, 1985.
26. J. L. Steger and D. S. Chaussee, 'Generation of body fitted coordinates using hyperbolic differential equations', *FSI Report 80-1*, Flow Simulations, Inc. Sunnyvale, CA, 1980.
27. T. H. Pulliam and J. L. Steger, 'On implicit finite-difference simulations of three-dimensional flow', *AIAA J.*, **18**, 159–167 (1980).
28. T. I.-P. Shih and W. J. Chyu, 'Approximate factorization with some terms', *AIAA J.*, **19**, 1759–1760 (1991).